



## Article

**Cite this article:** Konovalov YV (2025) Bragg scattering of surface-gravity waves by an ice shelf with rolling surface morphology. *Annals of Glaciology* **66**, e6, 1–13. <https://doi.org/10.1017/aog.2024.47>

Received: 1 May 2024

Revised: 1 December 2024

Accepted: 4 December 2024

**Keywords:**

abatement of incident ocean waves; bragg scattering; ice-shelf vibrations; ice shelf with periodic structure; ‘rolling’ morphology of the ice surface; under-shelf sea-water flux

Email: [yu-v-k@yandex.ru](mailto:yu-v-k@yandex.ru)

# Bragg scattering of surface-gravity waves by an ice shelf with rolling surface morphology

Yuri V. Konovalov 

Department of Mathematics, MIREA—Russian Technological University, Moscow, Russian Federation

**Abstract**

The propagation of elastic-flexural-gravity waves through an ice shelf is modeled using full three-dimensional elastic models that are coupled with a treatment of under-shelf sea-water flux: (i) finite-difference model (Model 1), (ii) finite-volume model (Model 2) and (iii) depth-integrated finite-difference model (Model 3). The sea-water flow under the ice shelf is described by a wave equation involving the pressure (the sea-water flow is treated as a “potential flow”). Numerical experiments were undertaken for an ice shelf with ‘rolling’ surface morphology, which implies a periodic structure of the ice shelf. The propagation of ocean waves through an ice shelf with rolling surface morphology is accompanied by Bragg scattering (also called Floquet band insulation). The numerical experiments reveal that band gaps resulting from this scattering occur in the dispersion spectra in frequency bands that are consistent with the Bragg’s law. Band gaps render the medium opaque to wave, that is, essentially, the abatement of the incident ocean wave by ice shelf with rolling surface morphology is observed in the models. This abatement explains the ability of preserving of ice shelves like the Ward Hunt Ice Shelf, Ellesmere Island, Canadian Arctic, from the possible resonant-like destroying impact of ocean swell.

**1. Introduction**

The Ward Hunt (west) Ice Shelf located near Ward Hunt Island, 83°6′0″ N; 74°10′0″ W on the north coast of Ellesmere Island, Nunavut, Canada, constitutes a ~50 m thick rim of landfast multi-year marine ice. The Ward Hunt Ice Shelf is not strictly an ice shelf in the sense commonly used in reference to Antarctic ice shelves, because it originates as multi-year landfast sea ice that has become immobile to the point of no longer drifting with wind and ocean current (Dowdeswell and Jeffries, 2017). Owing to this immobility, the Ward Hunt Ice Shelf represents a secure floating platform that allows observation of sea swell and other types of surface-gravity waves (e.g. impulsive waves generated from ridging, thermal fracturing, ‘micro tsunamis’ generated by ice-cliff calving, etc.) using broadband seismometers (Cathles and others, 2009). The concept of using ice-shelf platforms as observatories for sea swell in sea-ice covered waters is well supported in various Antarctic examples (e.g. Cathles and others, 2009; Bromirski and others, 2015; Cannata and others, 2019); however, the concept has never been tried before on ice shelves that fringe the Canadian Archipelago and Greenland. Seismometers have been deployed on embayed sea ice, for example in Svalbard; however, these deployments are at risk due to sea-ice breakup and drift (e.g. Serripietri and others, 2022).

Broadband seismographs deployed on floating ice shelves have the ability to observe a variety of oceanic and sea-ice phenomena, including sea swell (both locally generated and trans oceanic (Cathles and others, 2009; Tsai and McNamara, 2011), hydro acoustic signals (tremor) generated by colliding icebergs and sea ice floes (MacAyeal and others, 2008), impulsive waves generated by iceberg calving and sea-ice ridging (MacAyeal and others, 2009), ice quakes associated with sea-ice deformation and thermal fracturing of sea ice (Lewis and others, 1994) and superimposed ice layers (MacAyeal and others, 2019). In recent years, these observations have been used to demonstrate how seismological observation can define conventional properties such as sea-ice concentration and thickness (Cannata and others, 2019), as well as to infer difficult-to-observe properties such as the depth of snow superimposed on sea ice (e.g. Chaput and others, 2018; Schlindwein and others, 2020; Serripietri and others, 2022; Guillemot and others, 2021). An example of ice-shelf-deployed seismic data can be found in Cathles and others (2009).

The surface elevation of the now-diminished Ellesmere Ice Shelf and the Ward Hunt Ice Shelf consists of periodic waves, called ‘rolls’ by the European explorers who first described them (Hattersley-Smith and others, 1955; Hattersley-Smith, 1957). These rolls have an amplitude of meters and a wavelength of hundreds of meters. Rolls are rarely found on the ice shelves of the Antarctic, and only in limited areas, not the pervasive full coverage seen on the Ward Hunt Ice Shelf. Their origin is unknown, and many hypotheses have been offered to explain them (Jeffries, 2017; Coffey and others, 2022). Whatever their origin, the fact that they dominate an ice shelf that

© The Author(s), 2024. Published by Cambridge University Press on behalf of International Glaciological Society. This is an Open Access article, distributed under the terms of the Creative Commons Attribution licence (<http://creativecommons.org/licenses/by/4.0>), which permits unrestricted re-use, distribution and reproduction, provided the original article is properly cited.

[cambridge.org/aog](https://cambridge.org/aog)



grew from multi-year sea ice in the Last Ice Area, a region in the high latitudes of the Canadian Arctic and Greenland (e.g. Newton and others, 2021), demands attention. A hypothesis that we put forward is that the rolling surface morphology, created by whatever mechanism, offers an advantage to the survival of the multi-year sea ice which has this morphology. Specifically, the periodic variation of ice thickness creates ‘band gaps’, or frequency bands that prohibit the propagation of air- and water-coupled flexural-gravity waves (Freed-Brown and others, 2012; Nekrasov and MacAyeal, 2023). If the right frequencies of waves are prohibited from propagating through the ice shelf (they will be reflected at the ice front), it is possible that the band gap will protect the ice shelf from wave-flexure-induced damage and fracture.

The propagation of elastic-flexural waves through an ice shelf can be modeled by elastic models (e.g. Holdsworth and Glynn, 1978, among many others), based on elastic thin plate/elastic beam approximations. Some of these models consider coupled ice-shelf/sub-ice-shelf cavity systems (Holdsworth and Glynn, 1978; Sergienko, 2013, 2017; Papathanasiou and others, 2015, 2019; Meylan and others, 2017; Ilyas and others, 2018; Kalyanaraman and others, 2019, 2020; McNeil and Meylan, 2023; Bennetts and others, 2024) and permit estimation of possible effects of tides and ocean swell actions on the calving process. In particular, these models consider the eigenvalue problem for the ice-shelf/sub-ice sea-water systems (Holdsworth and Glynn, 1978; Papathanasiou and others, 2019), which is of interest in terms of possible resonances in the system. Further advancement of elastic-beam models occurred in the direction of viscoelastic rheological model development. In particular, tidal flexure of an ice shelf was obtained using the linear viscoelastic Burgers model (Reeh and others, 2003; Walker and others, 2013), nonlinear thin-plate viscoelastic model (MacAyeal and others, 2015) and the nonlinear 3-D viscoelastic full-Stokes model (Rosier and others, 2014). In particular, viscoelastic modeling provides a way (i) to explain the observed tidal flexure data and (ii) to explain the ice-shelf response to sudden changes in surface loads and applied bending moments (e.g. draining supraglacial lakes, iceberg calving, surface and basal crevassing).

Investigation of the modeled dispersion spectra reveals that the spectra obtained for an ice shelf with crevasses can be qualitatively different from the spectra in the case of no crevasses (Freed-Brown and others, 2012). Crevasses are widely distributed features in all ice shelves, and their appearance, growth and penetration are the subjects of many studies (e.g. van der Veen, 1998; van der Veen, 2002; Scambos and others, 2000). Essentially, the dispersion spectra obtained for a crevasse-ridden ice shelf reveal ‘band gaps’ that are absent from the spectra obtained for an ice shelf without crevasses. These band gaps are the frequency ranges over which no eigenmodes exist (Freed-Brown and others, 2012) and are a phenomenon that emerges when a wave is propagated through a periodic structure (Sheng, 2006). Band gaps arise in many different systems, including crystallography, photonic crystals, electron transport in metals and semiconductors (Ashcroft and Mermin, 1976), the formation of nearshore underwater sandbars (Mei, 1985), and gravity wave propagation through periodic structures of floating ice (Chou, 1998; Bennetts and Squire, 2009; Bennetts and others, 2009; Bennetts and Williams, 2010; Bennetts and Squire, 2012).

In this study, the propagation of elastic-flexural waves through an ice shelf with rolling surface morphology (Ward Hunt Ice Shelf morphology) was modeled using full three-dimensional (3-D) finite-difference elastic models that are coupled with a treatment of

under-shelf sea-water motion. These models differ in their approximation of the momentum equations: (i) Model 1 is based on the known differential form of the momentum equations and on the finite-difference approximation of the momentum equations (Konovalov, 2020, 2021b); (ii) Model 2 is based on the integral form of the momentum equations and the approximation of this form by the finite-volume method (Konovalov, 2023b, 2023c); (iii) Model 3 (Konovalov, 2021c) is based on the integrodifferential form of the momentum equations and on a finite-difference approximation of this form (in this model, the depth integration does not imply a thin plate approximation). In all three of these models, sea water under the ice shelf is treated as a homogeneously dense fluid, and the flow of water under the ice shelf is treated as a ‘potential flow’. The sea-water motion in all developed models is described by a wave equation involving the pressure, and it couples to the elastic motions of the ice through the pressure at the ice/water interface (Holdsworth and Glynn, 1978).

Numerical experiments show that ‘rolling’ surface morphology of the ice shelf, a distinctive feature of Arctic ice shelves along Ellesmere Island, can have a profound effect on how elastic-flexural waves propagate through the system. The experiments demonstrate that rolling surface morphology produces Bragg scattering (also called Floquet band insulation) that is potentially effective in preventing an incident wave from entering the ice shelf and causing subsequent fracture damage. The numerical results show frequency band gaps (band insulation) that are consistent with the Bragg’s law. The numerical results further indicate that these band gaps render the ice shelf/ocean system opaque to wave propagation with frequencies that fall within the range of the band gaps. By abating incident ocean wave activity, the rolling surface morphology inadvertently provides a fitness advantage to the ice shelf that protects it from damage.

## 2. Field equations

The 3-D elastic model is based on the well-known momentum equations (e.g. Landau and Lifshitz, 1986; Lurie, 2005):

$$\begin{cases} \frac{\partial \sigma_{xx}}{\partial x} + \frac{\partial \sigma_{xy}}{\partial y} + \frac{\partial \sigma_{xz}}{\partial z} = \rho \frac{\partial^2 U}{\partial t^2}; \\ \frac{\partial \sigma_{yx}}{\partial x} + \frac{\partial \sigma_{yy}}{\partial y} + \frac{\partial \sigma_{yz}}{\partial z} = \rho \frac{\partial^2 V}{\partial t^2}; \\ \frac{\partial \sigma_{zx}}{\partial x} + \frac{\partial \sigma_{zy}}{\partial y} + \frac{\partial \sigma_{zz}}{\partial z} = \rho \frac{\partial^2 W}{\partial t^2} + \rho g; \end{cases} \quad (1)$$

$$0 < x < L; y_1(x) < y < y_2(x); h_b(x, y) < z < h_s(x, y),$$

where (XYZ) is a rectangular coordinate system with  $x$ -axis along the central line (in the direction of wave propagation), and  $z$ -axis is pointing vertically upward;  $U$ ,  $V$  and  $W$  are two horizontal and one vertical ice displacements, respectively;  $\sigma$  is the stress tensor; and  $\rho$  is ice density. The ice shelf is of length  $L$  along the central line. The geometry of the ice shelf is assumed to be given by lateral boundary functions  $y_{1,2}(x)$  at sides labeled 1 and 2 and functions for the surface and base elevation,  $h_{s,b}(x, y)$ , denoted by subscripts  $s$  and  $b$ , respectively. Thus, the domain on which Eqns (1) are solved is  $\Omega = \{0 < x < L, y_1(x) < y < y_2(x), h_b(x, y) < z < h_s(x, y)\}$ .

Equation (1) can be rewritten in integrodifferential form. This integrodifferential form results from the vertical integration of the momentum Eqn (1) from the current vertical coordinate to the

ice surface. In particular, considering the first equation from Eqn (1) and integrating over  $z'$  from the current  $z$ -coordinate to  $h_s$  we obtain the following equation:

$$\int_z^{h_s} \frac{\partial \sigma_{xx}}{\partial x} dz' + \int_z^{h_s} \frac{\partial \sigma_{xy}}{\partial y} dz' + \sigma_{xz}|_{z=h_s} - \sigma_{xz} = \rho \int_z^{h_s} \frac{\partial^2 U}{\partial t^2} dz' \quad (2)$$

Next, using the Leibniz integral rule, we replace the first and second terms in Eqn (2) with the following, respectively.

$$\int_z^{h_s} \frac{\partial \sigma_{xx}}{\partial x} dz' = \frac{\partial}{\partial x} \int_z^{h_s} \sigma_{xx} dz' - (\sigma_{xx})_{z=h_s} \frac{\partial h_s}{\partial x}; \quad (3.1)$$

$$\int_z^{h_s} \frac{\partial \sigma_{xy}}{\partial y} dz' = \frac{\partial}{\partial y} \int_z^{h_s} \sigma_{xy} dz' - (\sigma_{xy})_{z=h_s} \frac{\partial h_s}{\partial y}. \quad (3.2)$$

Thus, instead of Eqn (2), we obtain the following equation:

$$\begin{aligned} \frac{\partial}{\partial x} \int_z^{h_s} \sigma_{xx} dz' + \frac{\partial}{\partial y} \int_z^{h_s} \sigma_{xy} dz' - (\sigma_{xx})_{z=h_s} \frac{\partial h_s}{\partial x} \\ - (\sigma_{xy})_{z=h_s} \frac{\partial h_s}{\partial y} + (\sigma_{xz})_{z=h_s} - \sigma_{xz} = \rho \int_z^{h_s} \frac{\partial^2 U}{\partial t^2} dz'. \end{aligned} \quad (4)$$

Taking in to account that the expression  $-(\sigma_{xx})_{z=h_s} \frac{\partial h_s}{\partial x} - (\sigma_{xy})_{z=h_s} \frac{\partial h_s}{\partial y} + (\sigma_{xz})_{z=h_s}$  is the  $x$ -component of the force  $\sqrt{\left(\frac{\partial h_s}{\partial x}\right)^2 + \left(\frac{\partial h_s}{\partial y}\right)^2 + 1}$  acting on a unit square of the ice surface (e.g. Landau and Lifshitz, 1986) and it is equal to zero according to the boundary conditions (ice surface is stress free), we finally obtain the following equation:

$$\frac{\partial}{\partial x} \int_z^{h_s} \sigma_{xx} dz' + \frac{\partial}{\partial y} \int_z^{h_s} \sigma_{xy} dz' - \sigma_{xz} = \rho \int_z^{h_s} \frac{\partial^2 U}{\partial t^2} dz'. \quad (5)$$

By performing similar manipulations with the second and third equations from Eqn (1), we obtain the following equations:

$$\frac{\partial}{\partial x} \int_z^{h_s} \sigma_{yx} dz' + \frac{\partial}{\partial y} \int_z^{h_s} \sigma_{yy} dz' - \sigma_{yz} = \rho \int_z^{h_s} \frac{\partial^2 V}{\partial t^2} dz' \quad (6)$$

and

$$\begin{aligned} \frac{\partial}{\partial x} \int_z^{h_s} \sigma_{xx} dz' + \frac{\partial}{\partial y} \int_z^{h_s} \sigma_{zy} dz' - \sigma_{zz} = \rho g (h_s - z) \\ + \rho \int_z^{h_s} \frac{\partial^2 W}{\partial t^2} dz'. \end{aligned} \quad (7)$$

Thus, by combining Eqns (5)–(7), we obtain the depth-integrated momentum equations, which are expressed as follows:

$$\begin{cases} \frac{\partial}{\partial x} \int_z^{h_s} \sigma_{xx} dz' + \frac{\partial}{\partial y} \int_z^{h_s} \sigma_{xy} dz' - \sigma_{xz} = \rho \int_z^{h_s} \frac{\partial^2 U}{\partial t^2} dz'; \\ \frac{\partial}{\partial x} \int_z^{h_s} \sigma_{yx} dz' + \frac{\partial}{\partial y} \int_z^{h_s} \sigma_{yy} dz' - \sigma_{yz} = \rho \int_z^{h_s} \frac{\partial^2 V}{\partial t^2} dz'; \\ \frac{\partial}{\partial x} \int_z^{h_s} \sigma_{zx} dz' + \frac{\partial}{\partial y} \int_z^{h_s} \sigma_{zy} dz' - \sigma_{zz} = \rho g (h_s - z) \\ + \rho \int_z^{h_s} \frac{\partial^2 W}{\partial t^2} dz'; \\ 0 < x < L; y_1(x) < y < y_2(x); h_b(x, y) < z < h_s(x, y). \end{cases} \quad (8)$$

Similar manipulations, for example, yield equations describing ice flow in a two-dimensional ice-flow model (Pattyn, 2000, 2002).

Sub-ice water flow is described by the the following wave equation (Holdsworth and Glynn, 1978):

$$\frac{\partial^2 W_b}{\partial t^2} = \frac{1}{\rho_w} \frac{\partial}{\partial x} \left( d_0 \frac{\partial P'}{\partial x} \right) + \frac{1}{\rho_w} \frac{\partial}{\partial y} \left( d_0 \frac{\partial P'}{\partial y} \right), \quad (9)$$

where  $\rho_w$  is the sea-water density;  $d_0(x, y)$  is the depth of the sub-ice water layer;  $W_b(x, y, t)$  is the vertical deflection of the ice-shelf base, and  $W_b(x, y, t) = W(x, y, h_b(x, y), t)$ ; and  $P'(x, y, t)$  is the deviation of the sub-ice water pressure from the hydrostatic value.

The boundary conditions for the ice shelf are (i) a stress-free ice surface; (ii) the normal stress exerted by sea water at the ice-shelf free edges and at the ice-shelf base; and (iii) rigidly fixed edges at the grounding line of the ice-shelf. Moreover, the linear combination of the boundary conditions (Konovalov, 2019) was also applied in the models considered in this study. This linear combination is expressed as

$$\alpha_1 F_i(U, V, W) + \alpha_2 \Phi_i(U, V, W) = 0, \quad i = 1, 2, 3, \quad (10)$$

where

- (i)  $F_i(U, V, W) = 0$  is the typical form of the boundary conditions, that is  $\sigma_{ik} n_k = f_i$ , where  $f_i$  is the given forcing on the boundary and  $\vec{n}$  is the unit vector normal to the surface;
- (ii)  $\Phi_i(U, V, W) = 0$  is the approximation based on integration of the typical form of the boundary conditions to the momentum equations (Eq (1) or Eq (8));
- (iii) the coefficients  $\alpha_1$  and  $\alpha_2$  satisfy the condition  $\alpha_1 + \alpha_2 = 1$ .

The boundary conditions for the sea-water layer correspond to the frontal incident wave. They are

- (i) at  $x = 0$ :  $\frac{\partial P'}{\partial x} = 0$ ;
- (ii) at  $y = y_1, y = y_2$ :  $\frac{\partial P'}{\partial y} = 0$ ;
- (iii) at  $x = L$ :  $P' = A_0 \rho_w g e^{i\omega t}$ , where  $A_0$  is the amplitude of the incident wave.

The full description of Model 1, based on Eqn (1), is presented in Konovalov (2019, 2020, 2021a, 2021b). Model 2 is based on the finite volume method of approximation of momentum equations (1) and is presented in Konovalov (2023b, 2023c). The full description of Model 3, based on Eqn (8), is presented in Konovalov (2021c, 2023a).

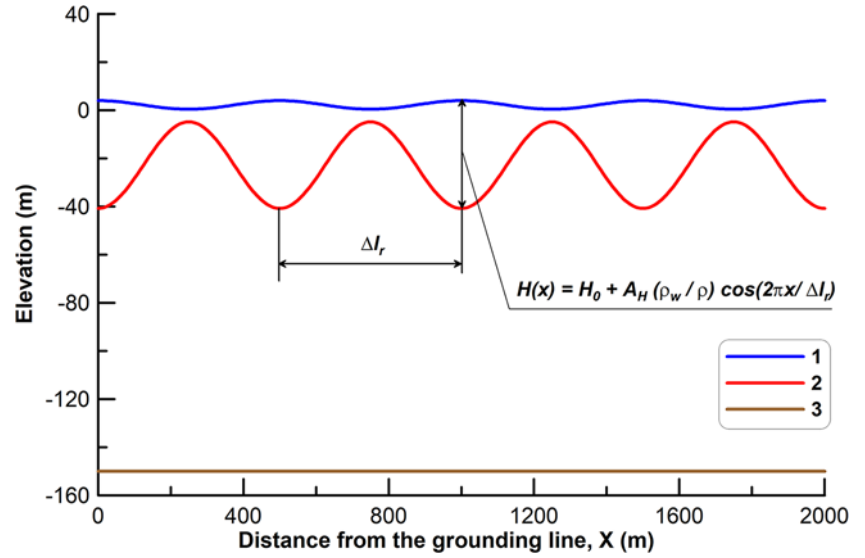


**Figure 1.** The ice-shelf and the cavity profiles considered in the numerical experiments. 1—ice-shelf surface; 2—ice-shelf base; 3—sea bottom. The amplitude of ice-thickness oscillations  $A_H = 18$  m. Spatial periodicity ( $\Delta l_r$ ) of the ‘rolls’ is equal to 0.5 km.

### 3. Model setup

The numerical experiments with forced vibrations were undertaken for a physically idealized ice shelf with the geometry shown in Figure 1. In the undeformed ice shelf, the four edges had coordinates  $x = 0$ ,  $x = L$ ,  $y_1 = 0$ ,  $y_2 = B$ , where  $L$  is the plate length along the  $x$ -axis and  $B$  is the plate width along the  $y$ -axis ( $B = y_2 - y_1$ , see Eqn (1)).

The ice plate had only one fixed edge (at  $x = 0$ ), while the other edges (at  $x = L$ ,  $y_1 = 0$ ,  $y_2 = B$ ) were free. This is the special case of an ice shelf, which is also known as an ‘ice tongue’ (e.g. Holdsworth and Glynn, 1978). The intact ice tongue was 2 km in longitudinal extent, 0.1–0.2 km width.

The ‘rolling’ surface morphology (Coffey and others, 2022) was modeled by sinusoidally varying ice thickness:

$$H(x) = H_0 + A_H \frac{\rho_w}{\rho} \cos\left(\frac{2\pi x}{\Delta l_r}\right), \quad (11)$$

where  $A_H$  is the amplitude of ice-thickness oscillations, which was considered as a parameter of the models;  $\Delta l_r$  is the spatial periodicity of the ‘rolls’ ( $\Delta l_r$  in the models was equal to 0.5 km);  $H_0$  in the models was equal to 25 m. Essentially, this ice tongue was considered as a part of the Ward Hunt Ice Shelf.

Taking into account the hydrostatic balance, the elevation of the ice surface  $h_s(x, y)$  and the elevation of the ice base  $h_b(x, y)$  are determined by the following equations, respectively:

$$h_s(x, y) = H \left(1 - \frac{\rho}{\rho_w}\right), \quad (12.1)$$

$$h_b(x, y) = -H \frac{\rho}{\rho_w}, \quad (12.2)$$

where  $H$  is the ice thickness (Eqn (11)).

That is, on the Ward Hunt Ice Shelf, both the ice surface and the ice base exhibited sinusoidal changes along the centerline (Fig. 1).

The water-layer depth in the case of the intact ice tongue also had sinusoidal variation (Fig. 1).

The periodic structure of the ice tongue is expected to provide Bragg scattering if the double spatial periodicity of the rolls  $2\Delta l_r$  is a multiple of the wavelength  $\lambda$ . Respectively, the Bragg wavenumbers  $k_b^{(n)}$ , at which we expect to observe band gaps in the modeled dispersion spectra, are expressed as

$$k_b^{(n)} = \frac{\pi n}{\Delta l_r}, \quad n = 1, 2, \dots \quad (13)$$

In all performed experiments, the physical properties of ice were defined by the following values: Young’s modulus,  $E = 9$  GPa, and Poisson’s ratio  $= 0.33$  (Schulson, 1999).

### 4. Numerical experiments

Numerical experiments were carried out using three models with different combinations of parameters  $\alpha_1$  and  $\alpha_2$  in Eqn (10). The results presented below were obtained using Model 1 for (i)  $\alpha_1 = 1$ ;  $\alpha_2 = 0$  and (ii)  $\alpha_1 = 0.2$ ;  $\alpha_2 = 0.8$ ; using Model 2 for (i)  $\alpha_1 = 1$ ;  $\alpha_2 = 0$  and (ii)  $\alpha_1 = 0$ ;  $\alpha_2 = 1$ ; and using Model 3 for  $\alpha_1 = 1$ ;  $\alpha_2 = 0$ .

The supplemental file contains the results obtained from the experiments performed using Models 1 and 3. Here are the results obtained using Model 2.

Figure 2 shows vertical deflections of the ice shelf. In general, using the second type of boundary conditions ( $\Phi_i(U, V, W)$  in Eqn (10)), the modeling reveal that the deflections are a superposition of a pure bending mode (Lamb-type mode) and a pure torsion mode (Fig. 2b). By determining the distances between the maxima/minima along the centerline deflection profile and then determining the average value, we obtain the wavelength and, accordingly, the wavenumber for a given periodicity  $T$  ( $T = \frac{2\pi}{\omega}$ , where  $\omega$  is the frequency of the forcing). Thus, we successively obtain a dispersion curve—the dependence of the wavenumber on the periodicity (or frequency) of the forcing (Fig. 3).

In Figure 3, dispersion curve 1 was obtained for the ice shelf with constant ice thickness (the case of  $A_H = 0$ ). In this case, the dispersion curve consists of sections of monotonic decrease, which are separated by intermode spaces (Figure 3) accompanying the transitions from the  $n + 1$  to the  $n$  bending Lamb-type mode. In the case of the rolling periodic geometry of the ice shelf (Fig. 1), the models yield the dispersion curves that have sections, where the typical relationship with monotonic decrease and intermode spaces is disturbed, as in dispersion curve 2 in Figure 3. In Figure 3, this section of curve 2 is the band gap, which occurs due to Bragg scattering and corresponds to the second Bragg wavenumber  $k_b^{(2)} \approx 12.57 \text{ km}^{-1}$ . Essentially, these sections with disturbed



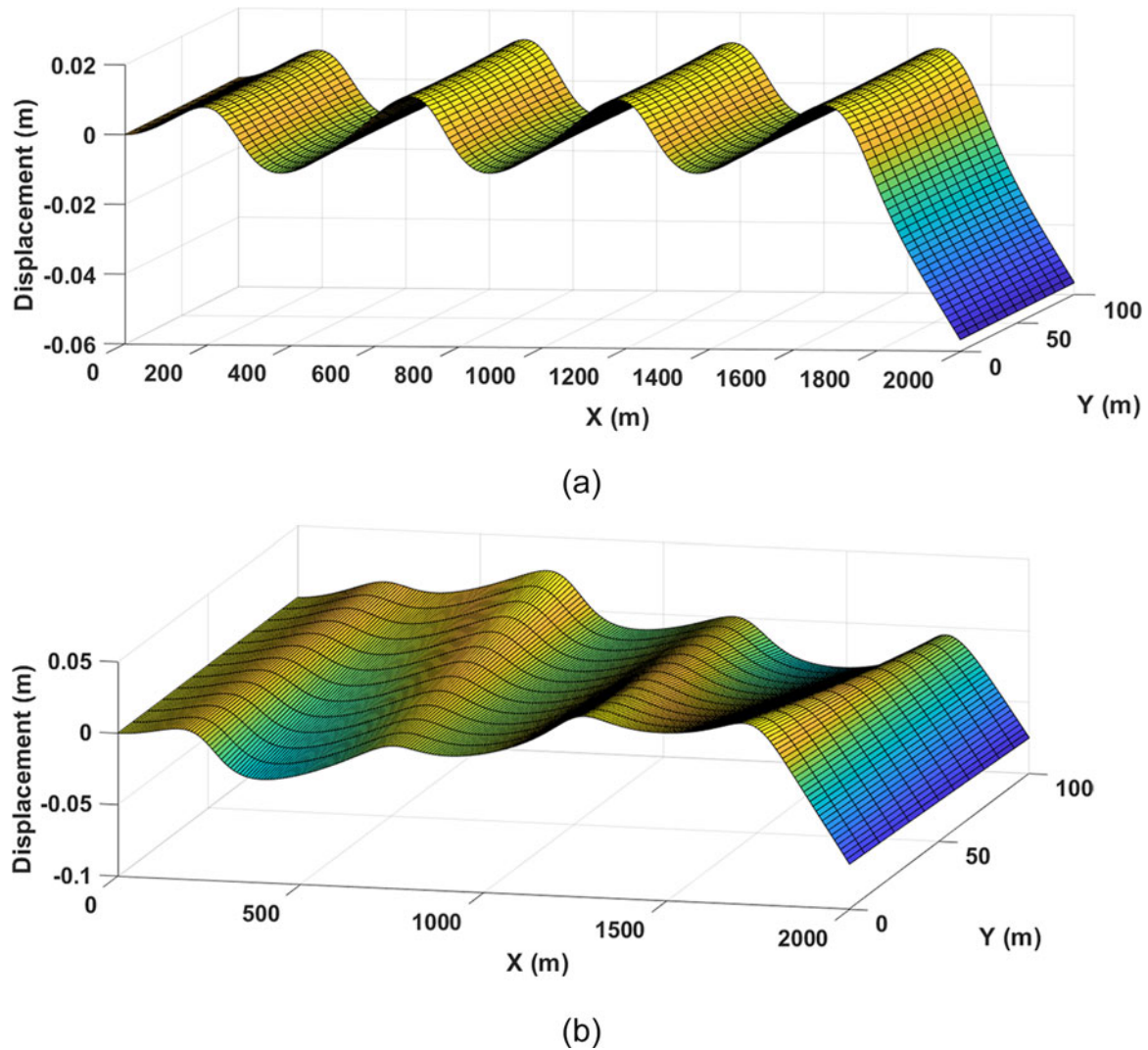


**Figure 2.** The vertical deflections of the ice shelf resulting from the impact of the frontal incident wave were obtained using Model 2 with the period of forcing  $T = 4$  s ( $T = \frac{2\pi}{\omega}$ ,  $\omega$  is the frequency of the forcing) in the case of (a)  $\alpha_1 = 1$ ,  $\alpha_2 = 0$  and (b)  $\alpha_1 = 0$ ,  $\alpha_2 = 1$ .

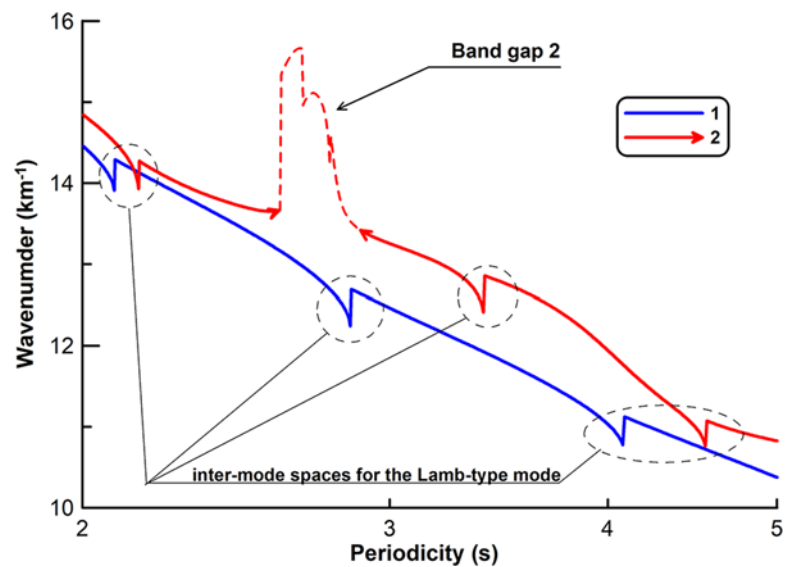


**Figure 3.** Dispersion spectra obtained using Model 2 with  $\alpha_1 = 1$ ,  $\alpha_2 = 0$  for ice shelf geometries differing in the amplitude of ice-thickness oscillations  $A_H$  (Figure 1): 1— $A_H = 0$  m; 2— $A_H = 10$  m. The arrowheads on the solid color line (curve 2) indicate the approximate positions of the left and right limits, which approximately define the left and right boundaries of the band gap. The dashed-colored line (in curve 2) indicates the perturbed wavenumber in the band gap. Similar arrowheads were also used in Figure 4 and other figures showing dispersion spectra to indicate of the boundaries of the band gaps.

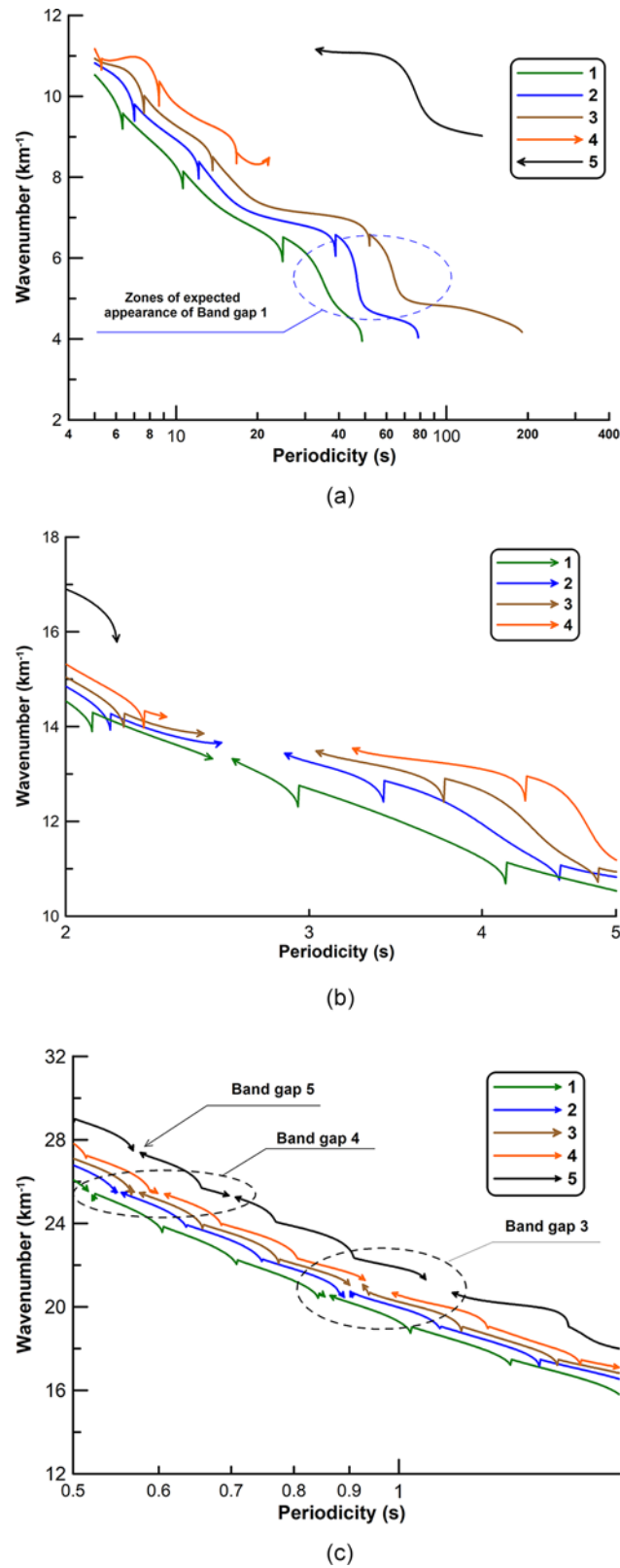


**Figure 4.** Dispersion spectra obtained using Model 2 with  $\alpha_1 = 1$ ,  $\alpha_2 = 0$  for ice-shelf geometries differing in the amplitude of ice-thickness oscillations  $A_H$  (Figure 1): 1— $A_H = 5$  m; 2— $A_H = 10$  m; 3— $A_H = 12$  m; 4— $A_H = 14$  m; 5— $A_H = 18$  m; (a) area of the expected first band gap; (b) area of the expected second band gap; (c) area of expected third and fourth band gaps. The arrowheads on the solid color lines indicate the approximate positions of the left and right boundaries of the band gap. The dashed-colored lines indicate the perturbed wavenumber in the band gap.

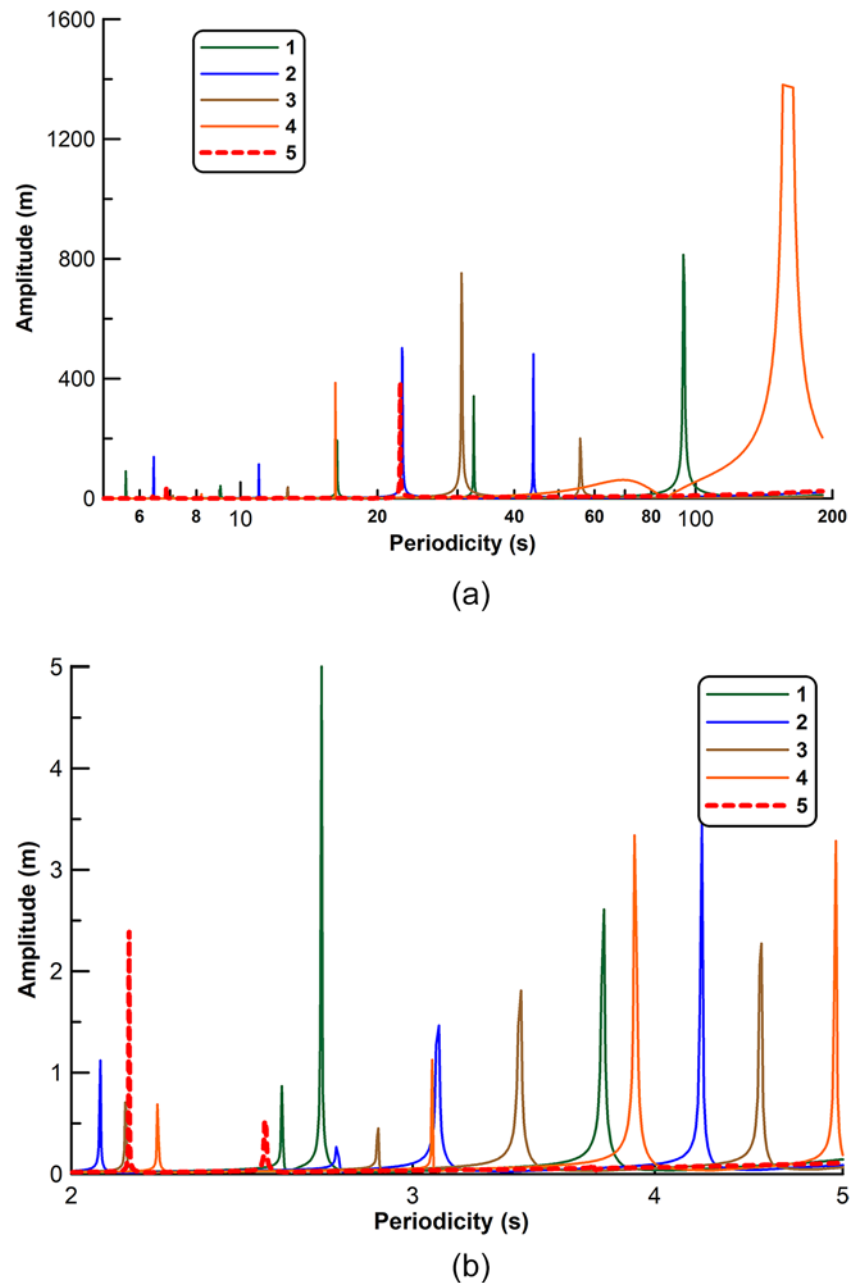


**Figure 5.** Amplitude spectra obtained using Model 2 with  $\alpha_1 = 1$ ,  $\alpha_2 = 0$  for ice-shelf geometries differing in the amplitude of ice-thickness oscillations  $A_H$  (Figure 1): 1– $A_H = 5$  m; 2– $A_H = 10$  m; 3– $A_H = 12$  m; 4– $A_H = 14$  m; 5– $A_H = 18$  m; (a) area of the expected first band gap (Figure 2a); (b) area of the expected second band gap (Figure 2b).

wavenumber values are defined by comparison with the typical relationship (curve 1 in Fig. 3).

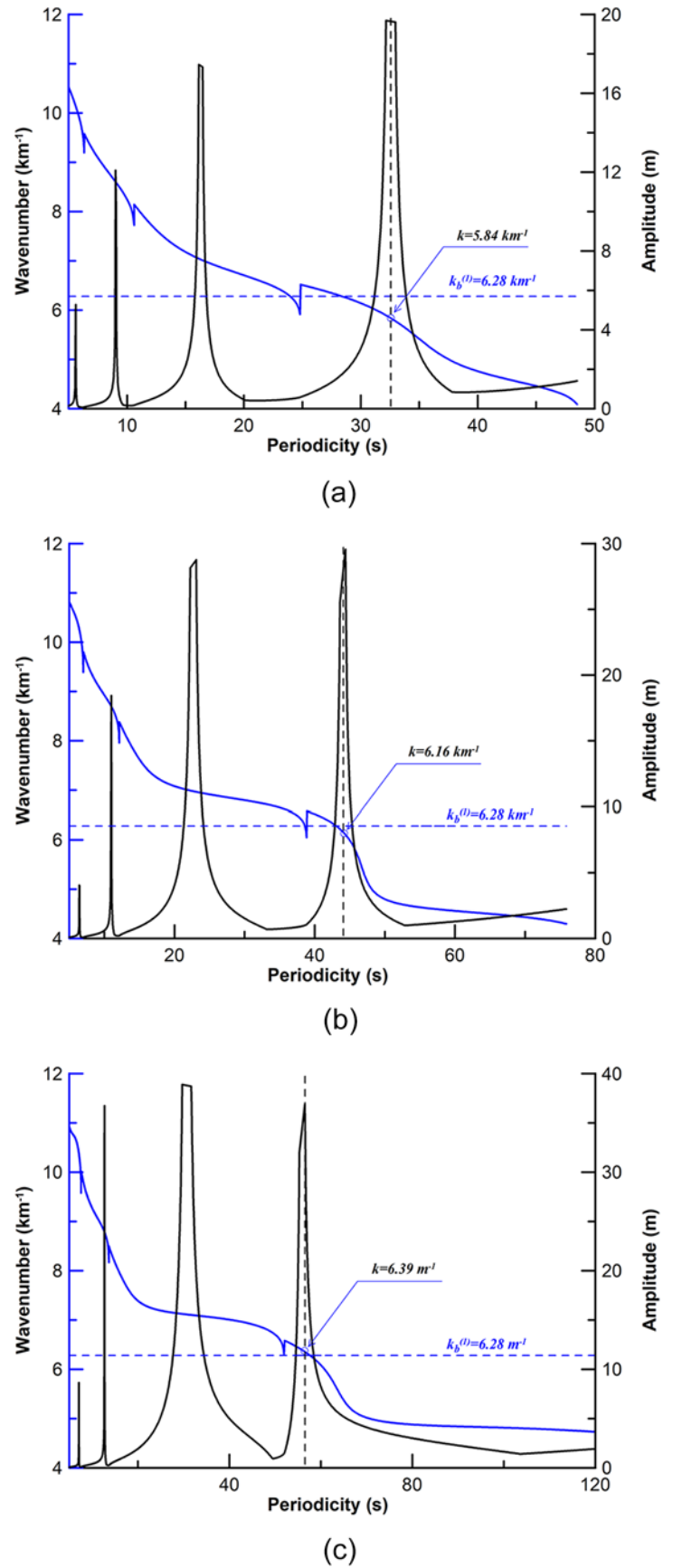
Experiments with ice shelves that have ‘rolling’ surface morphology revealed that there is the threshold value of the amplitude of ice-thickness oscillations ( $A_H$  in Eqn (11)), at which the band gaps appear in the dispersion spectra (Fig. 4a) (Konovalov, 2023a). Essentially, the amplitude of ice-thickness oscillations ( $A_H$ ) determines the depth of cavities at the base of the ice shelf that result from the ‘rolling’ morphology. These cavities are analogous to crevasses at the ice shelf base (Freed-Brown and others, 2012).

In Model 2, as in Model 1, the threshold value also depends on the Bragg wavenumber. The first band gap ( $k_b^{(1)} \approx 6.28 \text{ km}^{-1}$ ), appears in the spectrum at  $A_H/gt \approx 14$  m (Fig. 4a), that is, the first threshold value  $(A_H)_{th}^{(1)} \approx 14$  m. The second band gap ( $k_b^{(2)} \approx$

$12.57 \text{ km}^{-1}$ ), the third band gap ( $k_b^{(3)} \approx 19.04 \text{ km}^{-1}$ ) and the fourth band gap ( $k_b^{(4)} \approx 25.13 \text{ km}^{-1}$ ) appear in the spectrum at  $A_H/gt \approx 1$  m (Fig 4b and c), that is, the corresponding threshold values  $(A_H)_{th}^{(i)} \leq 1 \text{ m}$ ;  $i = 2, 3, 4$ .

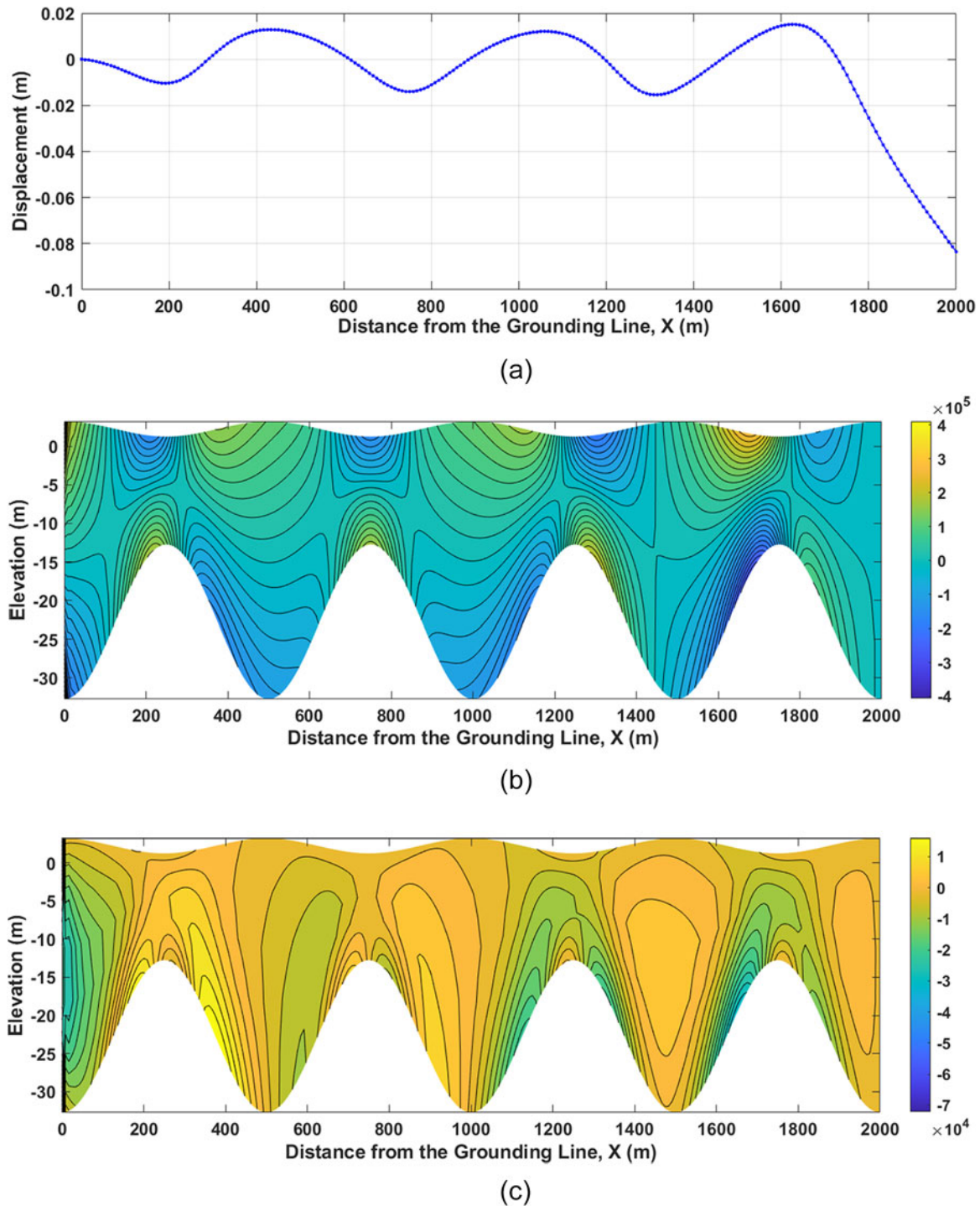
As in Model 1, the degradation of the amplitude spectrum (in terms of resonances abatement) is also observed at high  $A_H$  values, exceeding the threshold values  $(A_H)_{th}$  (Fig. 5). In particular, in the amplitude spectrum obtained at the value  $A_H = 18$  m, which corresponds to the observed fluctuations in ice thickness on the Ward Hunt Ice Shelf, starting from the impact periodicity  $T \approx 2.5$  s, there are no resonance peaks in the spectrum (Figure 5).

Figure 6 shows the alignment of the zone of the expected appearance of the first band gap ( $k_b^{(1)} \approx 6.28 \text{ km}^{-1}$ ) with the resonant peak in the corresponding range of periodicities of the forcing.



**Figure 6.** Dispersion spectrum and amplitude spectrum, including the area of the expected first band gap, obtained using Model 2 with  $\alpha_1 = 1$ ,  $\alpha_2 = 0$  for ice shelf geometries differing in the amplitude of ice-thickness fluctuations  $A_H$  (Figure 1): (a)  $A_H = 5 \text{ m}$ ; (b)  $A_H = 10 \text{ m}$ ; (c)  $A_H = 12 \text{ m}$ .





**Figure 7.** (a) Vertical displacement of ice  $W$  along the centerline due to the impact of the frontal incident wave. (b) Distribution of longitudinal stress ( $\sigma_{xx}$ ) in a vertical cross-section of the ice shelf along the centerline. (c) Distribution of shear stress ( $\sigma_{xz}$ ) in a vertical cross-section of the ice shelf along the centerline. The amplitude of ice-thickness oscillations  $A_H = 10$  m, the periodicity of forcing  $T = 5$  s. These distributions were obtained using Model 1 with  $\alpha_1 = 1$ ,  $\alpha_2 = 0$ .

In particular, (a) with the amplitude of ice-thickness fluctuations  $A_H$  equal to 5 m (Fig. 6a), the resonance peak is observed at the periodicity  $T_n \approx 32.54$  s (i.e.  $T_n \approx 32.54$  s is one of the eigenvalues), at which the wavenumber in the dispersion spectrum is about  $5.84 \text{ km}^{-1}$  (i.e.  $k_n \approx 5.84 \text{ km}^{-1}$ ); (b) with the amplitude of ice-thickness fluctuations  $A_H$  equal to 10 m (Fig. 6b), the resonance peak is observed at the

periodicity  $T_n \approx 44.04$  s, at which the wavenumber in the dispersion spectrum is about  $6.16 \text{ km}^{-1}$  (i.e.  $k_n \approx 6.16 \text{ km}^{-1}$ ); and (c) with the amplitude of ice-thickness fluctuations  $A_H$  equal to 12 m (Fig. 6c), the resonance peak is observed at the periodicity  $T_n \approx 55.92$  s, at which the wavenumber in the dispersion spectrum is about  $6.39 \text{ km}^{-1}$  (i.e.  $k_n \approx 6.39 \text{ km}^{-1}$ ). Respectively, the relative deviation of the corresponding

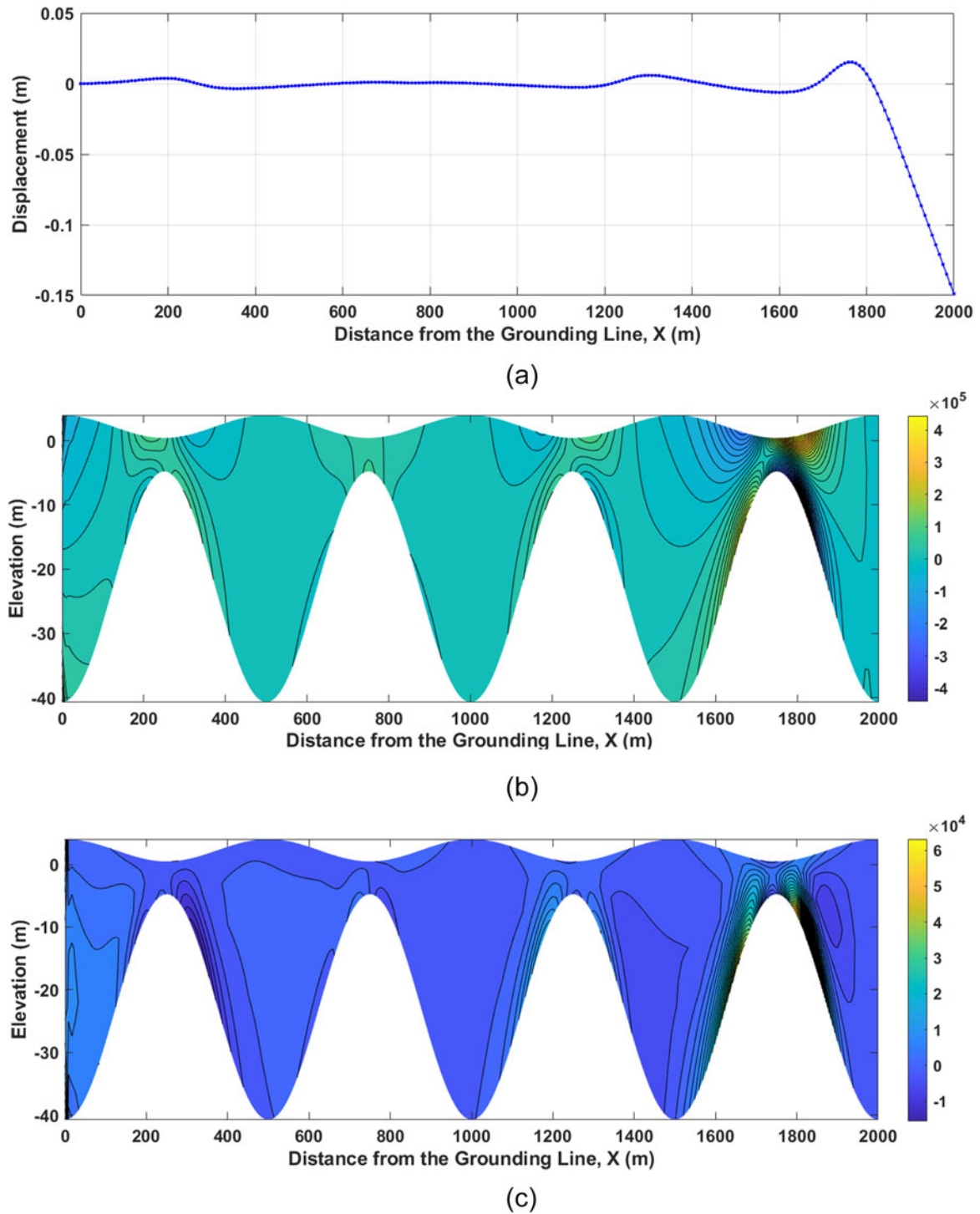


**Figure 8.** (a) Vertical displacement of ice  $W$  along the centerline due to the impact of the frontal incident wave. (b) Distribution of longitudinal stress ( $\sigma_{xx}$ ) in a vertical cross-section of the ice shelf along the centerline. (c) Distribution of shear stress ( $\sigma_{xz}$ ) in a vertical cross-section of the ice shelf along the centerline. The amplitude of ice-thickness oscillations  $A_H = 18$  m, the periodicity of forcing  $T = 5$  s. These distributions were obtained using Model 1 with  $\alpha_1 = 1$ ,  $\alpha_2 = 0$ .

wavenumber  $k_n$  from the first Bragg wavenumber  $k_b^{(1)}$  does not exceed 7%.

The distributions of longitudinal stresses ( $\sigma_{xx}$ ) (Figs 7b and 8b) reflect the distributions of vertical deformations along the central line of the ice shelf (Figs 7a and 8a). That is, the maxima/minima of longitudinal stresses coincide with maxima/minima of vertical deformations in the deformation profile (Figs 7a, b

and 8a, b). In particular, for a given eigenmode the distribution of longitudinal stresses has a specific periodic structure, in which the maxima/minima are aligned with the antinodes in the mode. Therefore, beyond the band gaps, the longitudinal stress distribution with a specific periodical structure (as in Fig. 7b) is the expected stress distribution in the ice shelf. Vice versa, inside the band gaps the distribution of longitudinal

stresses has a quasiperiodic or non-periodic structure (as in Fig. 8b).

The shear stress ( $\sigma_{xz}$ ) is an order of magnitude less than the longitudinal stress (Figs 7c and 8c). Beyond the band gaps, the maximum\minimum shear stress is usually observed at the grounding line, where in the models the ice shelf was considered rigidly fixed (Fig. 7c). Within the band gaps, the maximum\minimum shear stress is in most cases achieved in a vicinity of ice-shelf terminus, since the incident wave does not penetrate deeply into the ice shelf (Fig. 8c).

## 5. Discussion and conclusions

- (1) All suggested models reveal Bragg scattering for an ice shelf with a rolling surface morphology. The modeled Bragg scattering is expressed in the appearance of the anticipated band gaps in the dispersion spectra.

In Konovalov (2023a), it was established that there is a threshold value of crevasses depth, at which the first band gap (corresponding to the first Bragg wavenumber) appears in the spectra. For ice shelf with rolling surface morphology, the double amplitude of ice-thickness oscillations  $A_H$  is a parameter similar to the crevasse depth in a crevasse-ridden ice shelf (Freed-Brown and others, 2012). Accordingly, the threshold value of the amplitude  $(A_H)_{th}^{(1)}$ , at which the expected first band gap appears in the spectrum, also exists for the ice shelf with rolling surface morphology.

Analysis of the superposition of the dispersion spectrum and the amplitude spectrum allowed us to establish the following. The amplitude spectra contain resonance peaks corresponding to wavenumbers that are close to the first Bragg value  $k_b^{(1)} \approx 6.28 \text{ km}^{-1}$ . The appearance of Bragg scattering in a periodic structure, which also moves periodically with the same frequency, implies that the Bragg wavelength ( $\lambda_b^{(i)}$ ) and the amplitude of oscillations of the periodic structure ( $a$ ) satisfy the following condition:

$$a \ll \lambda_b^{(i)}. \quad (14)$$

In other words, Eqn (14) is the condition for the occurrence of the expected Bragg scattering in a periodically moving structure. Evidently, at resonance, condition (14) is not satisfied. In fact, condition (14) coincides with the condition for applying wave equation (Eqn 9).

Failure to satisfy condition (14) occurs not only when  $T = T_n$ , that is, when the periodicity of the incident wave coincides with the eigenvalue (when  $a \xrightarrow{T \rightarrow T_n} \infty$ ), but also when the periodicity of the forcing falls within the periodicity range containing  $T_n$  and which is defined by the width of the resonance peak. Therefore, the probability of the alignment of the expected band gap region with the periodicity range, in which the condition (14) is not satisfied, will be higher for a resonant peak with a larger width. The width of the resonance peaks in the amplitude spectra ( $A$  vs  $T$ ) increases with increasing periodicity of the forcing (Konovalov, 2019). Thus, the probability of the alignment is higher for the first Bragg value  $k_b^{(1)}$  than for the remaining  $k_b^{(i)}$ ,  $i = 2, 3 \dots$

These conclusions are confirmed by the results obtained in the present study. That is, the threshold value  $(A_H)_{th}^{(1)}$  for the appearance of the first band gap is higher than other threshold values  $(A_H)_{th}^{(i)}$ ,  $i = 2, 3 \dots$ . In particular, in Model 1 (with  $\alpha_1 = 1$ ,  $\alpha_2 = 0$ )  $(A_H)_{th}^{(1)} \approx 15 \text{ m}$ , but  $(A_H)_{th}^{(i)} < 1$ ,  $i = 2, 3, 4$ ; in Model 2 (with

$\alpha_1 = 1$ ,  $\alpha_2 = 0$ )  $(A_H)_{th}^{(1)} \approx 14 \text{ m}$  and  $(A_H)_{th}^{(i)} < 1$ ,  $i = 2, 3, 4$ ; in Model 2 (with  $\alpha_1 = 0$ ,  $\alpha_2 = 1$ )  $(A_H)_{th}^{(1)} \approx 15 \text{ m}$  and  $(A_H)_{th}^{(i)} \approx 2$ ,  $i = 2, 3, 4$ .

An increase in the amplitude of ice-thickness oscillations  $A_H$  (as an analogue of half the depth of ice crevasses in a crevasse-ridden ice shelf) yields shift in the resonance peaks (Konovalov, 2021a). Thus, a band gap appears in the dispersion spectrum, if the amplitude of ice-thickness oscillations  $A_H$  becomes higher than the threshold value  $(A_H)_{th}$ .

- (2) The torsional deformation component in the modes creates additional difficulties in treatment of the dispersion spectra, especially in Model 3, in which this component is observed in any case of the ratio  $\alpha_1/\alpha_2$  (see supplemental file). Essentially, the torsional deformation component yields additional intermode spaces (Konovalov, 2021a) in the dispersion spectra. These additional intermode spaces respectively provide transitions between torsional strain components in the modes and appear as discontinuities in the dispersion curves. Moreover, these discontinuities differ from the discontinuities accompanying the transitions between the components of the Lamb-type bending deformation in the modes, and can be considered, in particular, as a result of Bragg scattering if these discontinuities are located near the Bragg value. Thus, complementary investigation is required to correctly interpret the discontinuity in the dispersion curve. The investigation is based on the combination of dispersion and amplitude spectra (as shown in Fig. 6). Specifically, the discontinuities in the dispersion spectra corresponding to transitions between the torsional strain components in the modes and looking like band gaps, but not corresponding to Bragg scattering of the incident wave, coincide with the resonance peaks in the amplitude spectra (see section 4 in the supplemental file). In other words, these discontinuities, corresponding to transitions between the torsional strain components in the modes, are accompanied by a transition through resonances, while the band gaps corresponding to Bragg scattering are not accompanied by the same transition (see section (1) of this discussion). Thus, this spectral difference allows us to establish the type of discontinuity in the dispersion spectra.
- (3) In the models considered in this study, the band gap becomes the dominant effect and abates the resonances in the amplitude spectra if the amplitude of ice-thickness oscillations  $A_H$  exceeds the threshold value  $(A_H)_{th}$ . Thus, it can be said that the abatement of the incident wave by ice shelf with rolling surface/base morphology protects the ice shelf from dangerous resonant impact. For example, the range of periodicities, where the first band gap is observed (Fig. 4a), intersects with the range, where infragravity waves were observed: the range of periodicities is 50.250 s (Bromirski and others, 2010). That is, the first band gap, in particular, can protect the ice shelf from the impact of infragravity waves. This abatement may explain how multiyear sea ice in the Arctic Ocean along the coast of Ellesmere Island can be sufficiently stable and long-lived to evolve into the ice-shelf, once contiguous along the Ellesmere Island coast, reported by European and American explorers in the late 19th and early 20th centuries.

**Supplementary material.** The supplementary material for this article can be found at <https://doi.org/10.1017/aog.2024.47>.



**Data availability statement.** Full descriptions of the three models considered in this study are available on the Zenodo website.

1) Model 1:

<https://doi.org/10.5281/zenodo.4004338>

<https://doi.org/10.5281/zenodo.5562017>

2) Model 2:

<https://doi.org/10.5281/zenodo.7697142>

<https://doi.org/10.5281/zenodo.10252877>

3) Model 3:

<https://doi.org/10.5281/zenodo.5761719>

**Acknowledgements.** I thank Prof. Douglas R. MacAyeal for his helpful discussion of this manuscript and for the comments on this manuscript, which allowed for its improvement. I also thank Peter Nekrasov for his assistance in presenting preliminary results of this study at the AGU Fall Meeting 2022. Additionally, I am grateful to the editors of the *Annals of Glaciology*, Dr. Adrian Jenkins and Dr. Rachel Carr, as well as the two referees of this journal, for their comments on this manuscript that improved it.

## References

- Ashcroft NW and Mermin ND (1976) *Solid State Physics*. Books Cole: Belmont, California.
- Bennets L and Squire V (2009) Wave scattering by multiple rows of circular ice floes. *Journal of Fluid Mechanics* **639**, 213–238. doi: [10.1017/S0022112009991017](https://doi.org/10.1017/S0022112009991017)
- Bennets L and Williams T (2010) Wave scattering by ice floes and polynyas of arbitrary shape. *Journal of Fluid Mechanics* **662**, 5–35. doi: [10.1017/S0022112010004039](https://doi.org/10.1017/S0022112010004039)
- Bennetts LG, Biggs NRT and Porter D (2009) The interaction of flexural-gravity waves with periodic geometries. *Wave Motion* **46**(1), 57–73. doi: [10.1016/j.wavemoti.2008.08.002](https://doi.org/10.1016/j.wavemoti.2008.08.002)
- Bennetts LG and Squire VA (2012) On the calculation of an attenuation coefficient for transects of ice-covered ocean. *Proceedings of the Royal Society A* **468**, 136–162. doi: [10.1098/rspa.2011.0155](https://doi.org/10.1098/rspa.2011.0155)
- Bennetts LG, Williams TD and Porter R (2024) A thin-plate approximation for ocean wave interactions with an ice shelf. *Journal of Fluid Mechanics* **984**(A48). doi: [10.1017/jfm.2024.200](https://doi.org/10.1017/jfm.2024.200)
- Bromirski PD, Diez A, Gerstoft P, Stephen RA, Bolmer T, Wiens DA, Aster RC and Nyblade A (2015) Ross ice shelf vibrations. *Geophysical Research Letters* **42**, 7589–7597. doi: [10.1002/2015GL065284](https://doi.org/10.1002/2015GL065284)
- Bromirski PD, Sergienko O and MacAyeal DR (2010) Transoceanic infragravity waves impacting Antarctic ice shelves. *Geophysical Research Letters* **37**, 02502. doi: [10.1029/2009GL041488](https://doi.org/10.1029/2009GL041488)
- Cannata A, Cannavò F and Moschella S and others (2019) Exploring the link between microseism and sea ice in Antarctica by using machine learning. *Scientific Reports* **9**, 13050. doi: [10.1038/s41598-019-49586-z](https://doi.org/10.1038/s41598-019-49586-z)
- Cathles LM, IV, Okal EA and MacAyeal DR (2009) Seismic observations of sea swell on the floating Ross Ice Shelf, Antarctica. *Journal of Geophysical Research* **114**, F02015. doi: [10.1029/2007JF000934](https://doi.org/10.1029/2007JF000934)
- Chaput J, Aster RC, McGrath D, Baker M, Anthony RE and Gerstoft P and others (2018) Near-surface environmentally forced changes in the Ross Ice Shelf observed with ambient seismic noise. *Geophysical Research Letters* **45**(11), 187–196. doi: [10.1029/2018GL079665](https://doi.org/10.1029/2018GL079665)
- Chou T (1998) Band structure of surface flexural-gravity waves along periodic interfaces. *Journal of Fluid Mechanics* **369**, 333–350. doi: [10.1017/S002211209800192X](https://doi.org/10.1017/S002211209800192X)
- Coffey NB and 6 others (2022) Enigmatic surface rolls of the Ellesmere Ice Shelf. *Journal of Glaciology* **68**(271), 867–878. doi: [10.1017/jog.2022.3](https://doi.org/10.1017/jog.2022.3)
- Dowdeswell JA and Jeffries MO (2017) Arctic ice shelves: An introduction. In Copland L and Mueller D (eds), *Arctic Ice Shelves and Ice Islands*. Springer Polar Sciences, Springer: Dordrecht, 3–21. doi: [10.1007/978-94-024-1101-0\\_1](https://doi.org/10.1007/978-94-024-1101-0_1)
- Freed-Brown J, Amundson J, MacAyeal D and Zhang W (2012) Blocking a wave: Frequency band gaps in ice shelves with periodic crevasses. *Annals of Glaciology* **53**(60), 85–89. doi: [10.3189/2012AoG60A120](https://doi.org/10.3189/2012AoG60A120)
- Guillemot A and 6 others (2021) Modal sensitivity of rock glaciers to elastic changes from spectral seismic noise monitoring and modeling. *The Cryosphere* **15**, 501–529. doi: [10.5194/tc-15-501-2021](https://doi.org/10.5194/tc-15-501-2021)
- Hattersley-Smith G (1957) The rolls on the Ellesmere Ice Shelf. *Arctic* **10**(1), 32–44.
- Hattersley-Smith G, Crary AP and Christie RL (1955) Northern Ellesmere Island, 1953 and 1954. *Arctic* **8**(1), 3–36.
- Holdsworth G and Glynn J (1978) Iceberg calving from floating glaciers by a vibrating mechanism. *Nature* **274**, 464–466.
- Ilyas M, Meylan MH, Lamichhane B and Bennetts LG (2018) Time-domain and modal response of ice shelves to wave forcing using the finite element method. *Journal of Fluids and Structures* **80**, 113–131. doi: [10.1016/j.jfluidstructs.2018.03.010](https://doi.org/10.1016/j.jfluidstructs.2018.03.010)
- Jeffries MO (2017) The Ellesmere Ice Shelves, Nunavut, Canada. In Copland L and Mueller D ((eds)), *Arctic Ice Shelves and Ice Islands*. Springer Polar Sciences, Springer: Dordrecht. doi: [10.1007/978-94-024-1101-0\\_2](https://doi.org/10.1007/978-94-024-1101-0_2)
- Kalyanaraman B, Bennetts LG, Lamichhane B and Meylan MH (2019) On the shallow-water limit for modelling ocean-wave induced ice-shelf vibrations. *Wave Motion* **90**, 1–16. doi: [10.1016/j.wavemoti.2019.04.004](https://doi.org/10.1016/j.wavemoti.2019.04.004)
- Kalyanaraman B, Meylan MH, Bennetts LG and Lamichhane BP (2020) A coupled fluid-elasticity model for the wave forcing of an ice-shelf. *Journal of Fluids and Structures* **97**, 103074. doi: [10.1016/j.jfluidstructs.2020.103074](https://doi.org/10.1016/j.jfluidstructs.2020.103074)
- Kononov YV (2019) Ice-shelf vibrations modeled by a full 3-D elastic model. *Annals of Glaciology* **60**(79), 68–74. doi: [10.1017/aog.2019.9](https://doi.org/10.1017/aog.2019.9)
- Kononov YV (2020) Ice-shelf vibrations modeled by a full 3-D elastic model (Program Code) (Ver 2). Zenodo. doi: [10.5281/zenodo.4004338](https://doi.org/10.5281/zenodo.4004338)
- Kononov YV (2021a) Abatement of ocean-wave impact by crevasses in an ice shelf. *Journal of Marine Science and Engineering* **9**, 46. doi: [10.3390/jmse9010046](https://doi.org/10.3390/jmse9010046)
- Kononov YV (2021b) Ice-shelf vibrations modeled by a full 3-D elastic model (Version#3) (Patent). Zenodo. doi: [10.5281/zenodo.5562017](https://doi.org/10.5281/zenodo.5562017)
- Kononov YV (2021c) Ice-shelf vibrations modeled by a full 3-D elastic model (Version#4) (Patent). Zenodo. doi: [10.5281/zenodo.5761719](https://doi.org/10.5281/zenodo.5761719)
- Kononov YV (2023a) Modeling of ocean wave impacts on crevassed ice shelves. *Seismological Research Letters* **94**(3), 1526–1535. doi: [10.1785/0220220263](https://doi.org/10.1785/0220220263)
- Kononov YV (2023b) Ice-shelf vibrations modeled by a full 3-D elastic model (Version#5) (Patent). Zenodo. doi: [10.5281/zenodo.7697142](https://doi.org/10.5281/zenodo.7697142)
- Kononov YV (2023c) Ice-shelf vibrations modeled by a full 3-D elastic model (Version#6) (Patent). Zenodo. doi: [10.5281/zenodo.10252877](https://doi.org/10.5281/zenodo.10252877)
- Landau LD and Lifshitz EM (1986) *Course of Theoretical Physics, Vol. 7, Theory of Elasticity*, 3rd edn. Oxford: Butterworth-Heinemann, 187.
- Lewis CFM, Moore TC, Jr, Rea DK, Dettman DL, Smith AJ and Mayer LA (1994) Lakes of the Huron basin: Their record of runoff from the Laurentide Ice Sheet. *Quaternary Science Reviews* **13**, 891–922.
- Lurie AI (2005) *Theory of Elasticity*. Springer, Foundations of Engineering Mechanics: Berlin.
- MacAyeal DR, Banwell AF and Okal EA and others (2019) Diurnal seismicity cycle linked to subsurface melting on an ice shelf. *Annals of Glaciology* **60**(79), 137–157. doi: [10.1017/aog.2018.29](https://doi.org/10.1017/aog.2018.29)
- MacAyeal DR, Okal EA, Aster RC and Bassis JN (2008) Seismic and hydroacoustic tremor generated by colliding icebergs. *Journal of Geophysical Research* **113**, F03011. doi: [10.1029/2008JF001005](https://doi.org/10.1029/2008JF001005)
- MacAyeal DR, Okal EA, Aster RC and Bassis JN (2009) Seismic observations of glaciogenic ocean waves (micro-tsunamis) on icebergs and ice shelves. *Journal of Glaciology* **55**(190), 193–206. doi: [10.3189/002214309788608679](https://doi.org/10.3189/002214309788608679)
- MacAyeal D, Sergienko O and Banwell A (2015) A model of viscoelastic ice-shelf flexure. *Journal of Glaciology* **61**(228), 635–645. doi: [10.3189/2015JoG14J169](https://doi.org/10.3189/2015JoG14J169)

- McNeil S and Meylan MH (2023) Time-dependent modelling of the wave-induced vibration of ice shelves. *Journal of Marine Science and Engineering* **11**, 1191. doi: [10.3390/jmse11061191](https://doi.org/10.3390/jmse11061191)
- Mei CC (1985) Resonant reflection of surface water waves by periodic sandbars. *Journal of Fluid Mechanics* **152**, 315–335. doi: [10.1017/S0022112085000714](https://doi.org/10.1017/S0022112085000714)
- Meylan M, Bennetts L, Hosking R and Catt E (2017) On the calculation of normal modes of a coupled ice-shelf/sub-ice-shelf cavity system. *Journal of Glaciology* **63**(240), 751–754. doi: [10.1017/jog.2017.27](https://doi.org/10.1017/jog.2017.27)
- Nekrasov P and MacAyeal DR (2023) Ocean wave blocking by periodic surface rolls fortifies Arctic ice shelves. *Journal of Glaciology*, 1–11. doi: [10.1017/jog.2023.58](https://doi.org/10.1017/jog.2023.58)
- Newton R, Pfirman S, Tremblay LB and DeRepentigny P (2021) Defining the “ice shed” of the Arctic Ocean’s last ice area and its future evolution. *Earth’s Future* **9**, e2021EF001988. doi: [10.1029/2021EF001988](https://doi.org/10.1029/2021EF001988)
- Papathanasiou TK, Karperaki AE and Belibassakis KA (2019) On the resonant hydroelastic behaviour of ice shelves. *Ocean Modelling* **133**, 11–26. doi: [10.1016/j.ocemod.2018.10.008](https://doi.org/10.1016/j.ocemod.2018.10.008)
- Papathanasiou TK, Karperaki AE, Theotokoglou EE and Belibassakis KA (2015) Hydroelastic analysis of ice shelves under long wave excitation. *Natural Hazards and Earth System Sciences* **15**, 1851–1857. doi: [10.5194/nhess-15-1851-2015](https://doi.org/10.5194/nhess-15-1851-2015)
- Pattyn F (2000) Ice-sheet modeling at different spatial resolutions: Focus on the grounding zone. *Annals of Glaciology* **31**, 211–216. doi: [10.3189/172756400781820435](https://doi.org/10.3189/172756400781820435)
- Pattyn F (2002) Transient glacier response with a higher-order numerical ice-flow model. *Journal of Glaciology* **48**(162), 467–477. doi: [10.3189/172756502781831278](https://doi.org/10.3189/172756502781831278)
- Reeh N, Christensen EL, Mayer C and Olesen OB (2003) Tidal bending of glaciers: A linear viscoelastic approach. *Annals of Glaciology* **37**, 83–89. doi: [10.3189/172756403781815663](https://doi.org/10.3189/172756403781815663)
- Rosier SHR, Gudmundsson GH and Green JAM (2014) Insights into ice stream dynamics through modeling their response to tidal forcing. *The Cryosphere* **8**, 1763–1775. doi: [10.5194/tc-8-1763-2014](https://doi.org/10.5194/tc-8-1763-2014)
- Scambos TA, Hulbe C, Fahnestock M and Bohlander J (2000) The link between climate warming and break-up of ice shelves in the Atlantic Peninsula. *Journal of Glaciology* **46**(154), 516–530. doi: [10.3189/172756500781833043](https://doi.org/10.3189/172756500781833043)
- Schlindwein VSN, Henning K, Hiller M, Scholz J-R and Schmidt-Aursch MC (2020) First Ocean Bottom Seismometer network underneath the ice-covered Arctic Ocean: Operational challenges and chances for monitoring the state of the sea ice cover. *AGU Fall Meeting 2020*, poster S055-0005.
- Schulson EM (1999) The structure and mechanical behavior of Ice. *Jom* **51**(2), 21–27. doi: [10.1007/s11837-999-0206-4](https://doi.org/10.1007/s11837-999-0206-4)
- Sergienko O (2013) Normal modes of a coupled ice-shelf/sub-ice-shelf cavity system. *Journal of Glaciology* **59**(213), 76–80. doi: [10.3189/2013JoG12J096](https://doi.org/10.3189/2013JoG12J096)
- Sergienko OV (2017) Behavior of flexural gravity waves on ice shelves: Application to the Ross Ice Shelf. *Journal of Geophysical Research: Oceans* **122**(8), 6147–6164. doi: [10.1002/2017JC012947](https://doi.org/10.1002/2017JC012947)
- Serripietri A, Moreau L, Boue P, Weiss J and Roux P (2022) Recovering and monitoring the thickness, density, and elastic properties of sea ice from seismic noise recorded in Svalbard. *The Cryosphere* **16**, 2527–2543. doi: [10.5194/tc-16-2527-2022](https://doi.org/10.5194/tc-16-2527-2022)
- Sheng P (2006) *Introduction to Wave Scattering, Localization and Mesoscopic Phenomena*. Springer: Berlin.
- Tsai VC and McNamara DE (2011) Quantifying the influence of sea ice on ocean microseism using observations from the Bering Sea, Alaska. *Geophysical Research Letters* **38**, L22502. doi: [10.1029/2011GL049791](https://doi.org/10.1029/2011GL049791)
- van der Veen CJ (1998) Fracture mechanics approach to penetration of bottom crevasses on glaciers. *Cold Regions Science and Technology* **27**(3), 213–223. doi: [10.1016/S0165-232X\(98\)00006-8](https://doi.org/10.1016/S0165-232X(98)00006-8)
- van der Veen CJ (2002) Calving glaciers. *Progress in Physical Geography: Earth and Environment* **26**(1), 96–122. doi: [10.1191/0309133302pp327ra](https://doi.org/10.1191/0309133302pp327ra)
- Walker RT, Parizek BR, Alley RB, Anandakrishnan S, Riverman KL and Christianson K (2013) Ice-shelf tidal flexure and subglacial pressure variations. *Earth and Planetary Science Letters* **361**, 422–428. doi: [10.1016/j.epsl.2012.11.008](https://doi.org/10.1016/j.epsl.2012.11.008)